IEEE Photonics Journal
An IEEE Photonics Society Publication

Open Access

Influence of Temperature on All-Silica Fabry-Pérot Pressure Sensor

Volume 13, Number 3, June 2021

Jintao Chen
Heming Wei
Liang Zhang
Zhifeng Wang
Guilin Zhang
Zhenyi Chen
Tingyun Wang
Fufei Pang

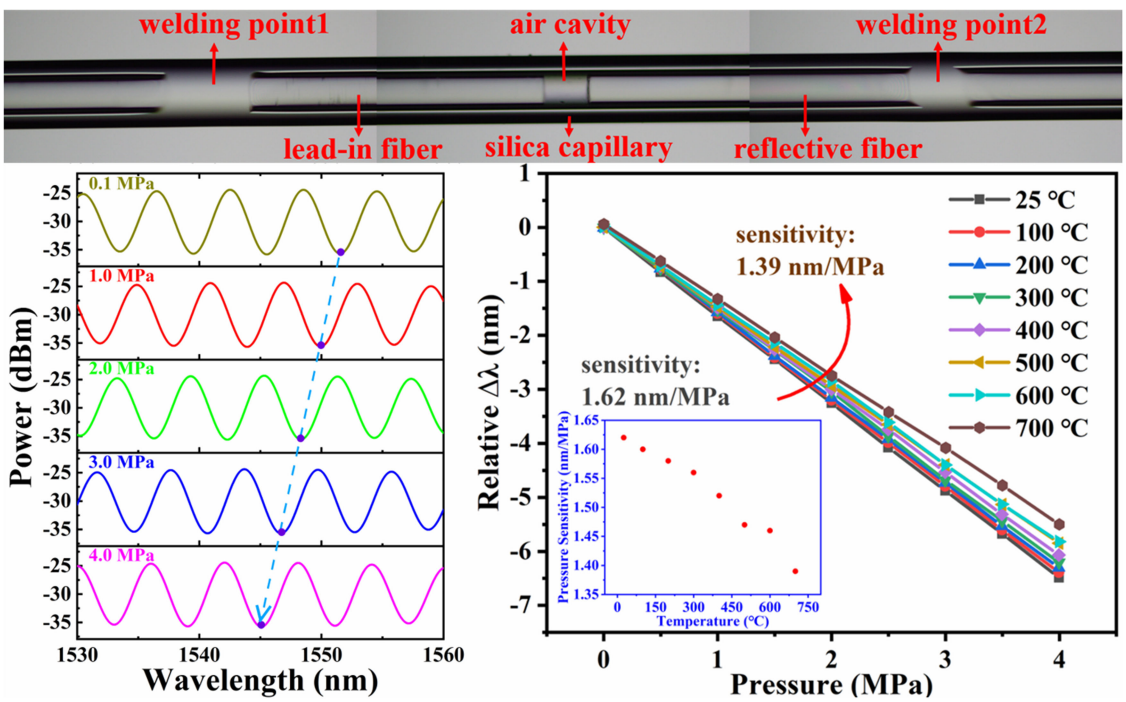

DOI: 10.1109/JPHOT.2021.3083808

Influence of Temperature on All-Silica Fabry-Pérot Pressure Sensor

Jintao Chen,[1] Heming Wei,[1] Liang Zhang,[1] Zhifeng Wang,[1] Guilin Zhang,[2] Zhenyi Chen,[1] Tingyun Wang,[1] and Fufei Pang[1]

[1]Key Laboratory of Specialty Fiber Optics and Optical Access Networks, Joint International Research Laboratory of Specialty Fiber Optics and Advanced Communication, Shanghai University, Shanghai 200444, China
[2]Leishier Photoelectric Information Engineering Company, Ltd, Wuhan 430205, China

DOI:10.1109/JPHOT.2021.3083808

Manuscript received April 8, 2021; revised May 20, 2021; accepted May 21, 2021. Date of publication May 26, 2021; date of current version June 22, 2021. This work was supported by the National Natural Science Foundation of China under Grants 61735009, 61975108 and 62005153. Corresponding author: Fufei Pang (e-mail: ffpang@shu.edu.cn.)

Abstract: An all-silica Fabry-Pérot interferometer (FPI) is demonstrated for high-temperature pressure monitoring. The pressure sensor is fabricated with single mode fiber and silica capillary by CO_2 laser. Owing to slight mismatch of thermal expansion coefficient in all-silica structure, it can work stably under 600°C atmosphere. The influence of the temperature on the pressure sensor was investigated within a temperature range from 25°C to 700°C and a pressure range from standard atmosphere pressure to 4 MPa. The experimental results show that the wavelength shift versus the pressure at each temperature is linear, which indicates the proposed FPI pressure sensor has potential applications in industrial reactors, oil and gas wells, and so on.

Index Terms: Fabry-Pérot, pressure sensor, high-temperature.

1. Introduction

Fiber-optic pressure sensor has found many applications in the fields of aircraft, oil field, nuclear power, *etc*. It can be used for pressure sensing with the advantages of immunity to electromagnetic interference, small size, corrosion resistance, electrical insulation and remote detection [1]–[7]. Numerous fiber-optic pressure sensors based on different mechanisms have been proposed. Particularly, the fiber-optic pressure sensors based on Fabry-Pérot interferometers (FPIs) have attracted much interest of the researchers because of the stable performance for pressure monitoring, high pressure sensitivity and so on. FPI pressure sensors can be divided into two types, including intrinsic Fabry-Pérot interferometers (IFPIs) [8], [9] and extrinsic Fabry-Pérot interferometers (EFPIs) [10], [11]. Specially, the ultraviolet (UV) adhesive is proposed to be utilized in IFPI pressure sensors due to its high elastic coefficient, which can be deformed easily under the pressure [8], [9]. The fabricated UV adhesive based pressure sensors have been demonstrated with the sensitivity of 475 pm/MPa [8] and 1.13 nm/MPa around 1560 nm [9]. However, they could be only used in the room temperature environment limited by the UV adhesive's tolerable temperature. Compared with IFPIs, EFPIs have advantages of low temperature cross-sensitivity, high tolerable temperature, *etc*. Plenty of methods were carried out to fabricate high-temperature pressure EFPIs, such as arc discharge technology [12], [13], diaphragm-coated technology [14], [15], chemical or femtosecond

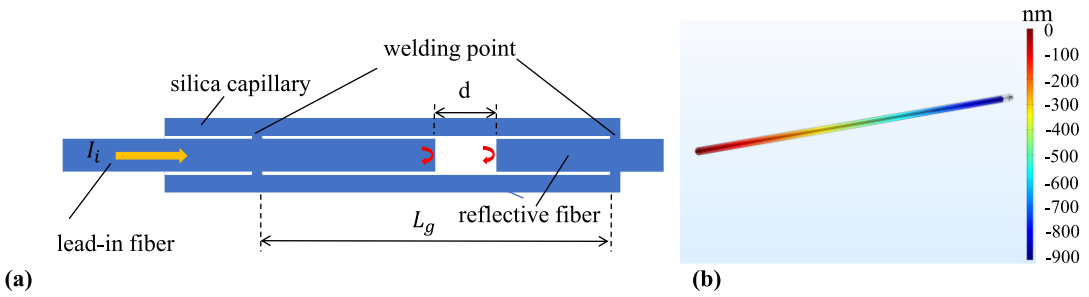

Fig. 1. (a) Schematic of the sensor structure; (b) the sensor's state under 4 MPa gas pressure at room temperature simulated by COMSOL software.

(fs) laser etched technology [16]–[18], *etc*. However, all these methods mentioned above need several steps to get thin diaphragms, either physical polishing, chemical or fs laser processing, which would make the sensor fabrication sophisticated. Afterwards, Qi *et al.* proposed a kind of pressure sensors without the diaphragm used in the oil or gas well, which are fabricated more easily [19]. Zhao *et al.* packaged the sensors with metal protective bodies to protect them [11]. The packaged sensor could tolerate high pressure up to 69 MPa owing to its diaphragm-free structure while it needs to cascade a fiber Bragg grating (FBG) to compensate the temperature when it is applied in ∼100°C environment. Up to date, the influence of the temperature on the performance of the pressure sensor was rarely investigated.

In this paper, an all-silica EFPI pressure sensor was fabricated by CO_2 laser fusion without any other adhesive, which can work stably at 600°C to measure the surrounding pressure with a pressure sensitivity of 1.46 nm/MPa. Pressure tests were carried out from 25°C to 700°C with a range from standard atmosphere pressure to 4 MPa. The experimental results show that the relative wavelength shift is linearly proportional to the pressure with the temperature-dependent sensitivity, which decreases from 1.62 nm/MPa at 25°C to 1.39 nm/MPa at 700°C. It offers potentials for pressure sensing, like gas or fluid pressure monitoring in the fields with high-temperature scenario.

2. Principle and Simulation

Fig. 1(a) shows the structure of the pressure sensor, which is made up of three parts: lead-in fiber, reflective fiber and a section of capillary. There is an air Fabry-Pérot cavity between the lead-in fiber and the reflective fiber. The lead-in fiber is used to transmit the incident light and the reflective light from the FP cavity. The capillary is used to seal and fix the two fibers, which has an inner diameter of 130 μm and an outer diameter of 310 μm. The cladding diameter of single mode fiber (SMF) is 125 μm so that it can be inserted into the capillary.

For the FP cavity, the reflective light I_r can be written as:

$$I_r = R_1 + R_2 \cdot (1 - R_1)^2 - 2 \cdot \sqrt{R_1 \cdot R_2} \cdot (1 - R_1) \cdot \cos\left(\frac{4 n_a \pi d}{\lambda}\right) \tag{1}$$

where R_1 and R_2 are the reflective coefficients of the two mirrors of the cavity, n_a is the refractive index of air, d is the cavity length and λ is the light wavelength, respectively. Once R_1, R_2 and λ are fixed, the reflective signal only varies with the cavity length d.

When the ambient pressure is applied on the FP sensor, the capillary will be deformed. The air cavity length variation Δd can be obtained as [20]:

$$\Delta d = \frac{L_g \cdot r_o^2 \cdot (1 - 2\mu)}{E(r_o^2 - r_i^2)} \cdot \Delta P \tag{2}$$

where ΔP is the pressure difference between the outer and inner part of the sensor, L_g is the distance between two fusion points, r_o is the outer radius, r_i is the inner radius of the silica capillary, E is the Young's modulus of the silica material and μ is the Poisson's ratio of the capillary, respectively. Equation (2) can be divided into two parts. One is the lateral pressure's effect to cavity length change, which lengthens the cavity length as:

$$\Delta d_1 = \frac{2\mu L_g}{E} \cdot \frac{\Delta P \cdot r_o^2}{r_o^2 - r_i^2} \tag{3}$$

The other one is the axial pressure's effect to cavity length change, which shortens the cavity length as:

$$\Delta d_2 = \frac{L_g}{E} \cdot \frac{\Delta P \cdot r_o^2}{r_o^2 - r_i^2} \tag{4}$$

The thinner the capillary wall is, and the longer the fusion-point distance L_g is, the larger the pressure sensitivity becomes. Between them, L_g is the main factor that affects the pressure sensitivity. Δd_1 is the elongate cavity length by the lateral pressure while Δd_2 is the shortened cavity length by the axial pressure. As a result, the total cavity length change $\Delta d = \Delta d_2 - \Delta d_1$. According to Eqs. (3) and (4), it can be deduced that, $\Delta d_2 / \Delta d_1 = 1/2\mu \approx 3$ (the Poisson's ratio of silica material μ is 0.17). It indicates that the axial pressure plays the dominant role in affecting the cavity length. Fig. 1(b) is the sensor's state under 4 MPa gas pressure at the room temperature simulated by a commercial simulation software (COMSOL Multiphysics). It shows that the sensor is compressed in the axial direction.

Here, the relationship between the cavity length and the free spectral range (FSR) is written as:

$$FSR = \frac{\lambda^2}{2n_a d} \tag{5}$$

where λ is the working wavelength. Thus, the FSR corresponding to the air cavity (200 μm) around 1550 nm is 6.01 nm.

The pressure is measured by measuring the optical path difference (OPD) of the air cavity:

$$\Delta OPD = 2d - 2(d - \Delta d) = 2 \cdot \Delta d \tag{6}$$

The interference mechanism of the FPI sensor is that the variation of the OPD is proportional to the relative wavelength shift $\Delta\lambda$. Therefore, the relationship between the relative $\Delta\lambda$ and the pressure difference ΔP can be written as:

$$\Delta\lambda = \frac{\Delta OPD}{OPD}\lambda = \frac{2 \cdot \frac{L_g \cdot r_o^2 \cdot (1-2\mu)}{E(r_o^2 - r_i^2)} \cdot \Delta P \cdot \lambda}{2d} = \frac{L_g \cdot r_o^2 \cdot (1-2\mu) \cdot \lambda}{E \cdot d(r_o^2 - r_i^2)} \cdot \Delta P \tag{7}$$

As for the silica material in the room temperature, $E = 72.99GPa$, $\mu = 0.17$. L_g, r_o and r_i can be considered to be constant because there is only slight variation when applying pressure. The theoretical pressure sensitivity is about 1.70 nm/MPa according to Eq. (7).

Besides, the pressure sensing characteristic of the sensor was simulated from standard atmosphere pressure to 4 MPa with a temperature range from 25°C to 700°C with a step of 100°C. As shown in Fig. 2(a), the pressure sensitivity decreases from 1.74 nm/MPa at 25°C to 1.55 nm/MPa at 700°C. Fig. 2(b) displays the decreasing tendency of the pressure sensitivity and the increasing trend of the silica material's Young's modulus with the temperature increasing. Note that the sensitivity of the pressure sensor essentially refers the absolute value of the slope of the sensitivity curves. The data of Young's modulus against the temperature is obtained by the COMSOL software. From Eq. (7), one can obtain that the relative $\Delta\lambda$ would decrease when Young's modulus E increases as the residual parameters are fixed. Consequently, the pressure sensitivity decreases with the increased temperature.

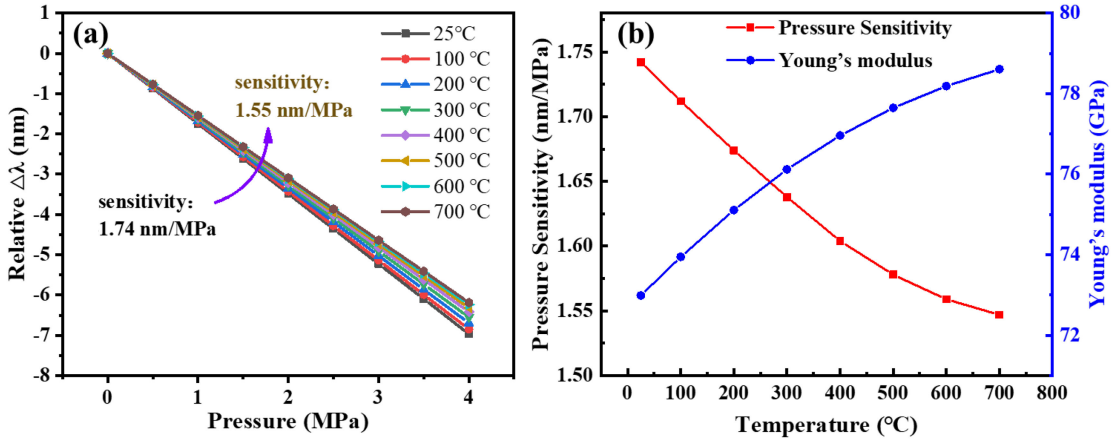

Fig. 2. (a) The pressure simulation results at different temperatures; (b) the pressure sensitivity and the Young's modulus of the silica material versus the increased temperature.

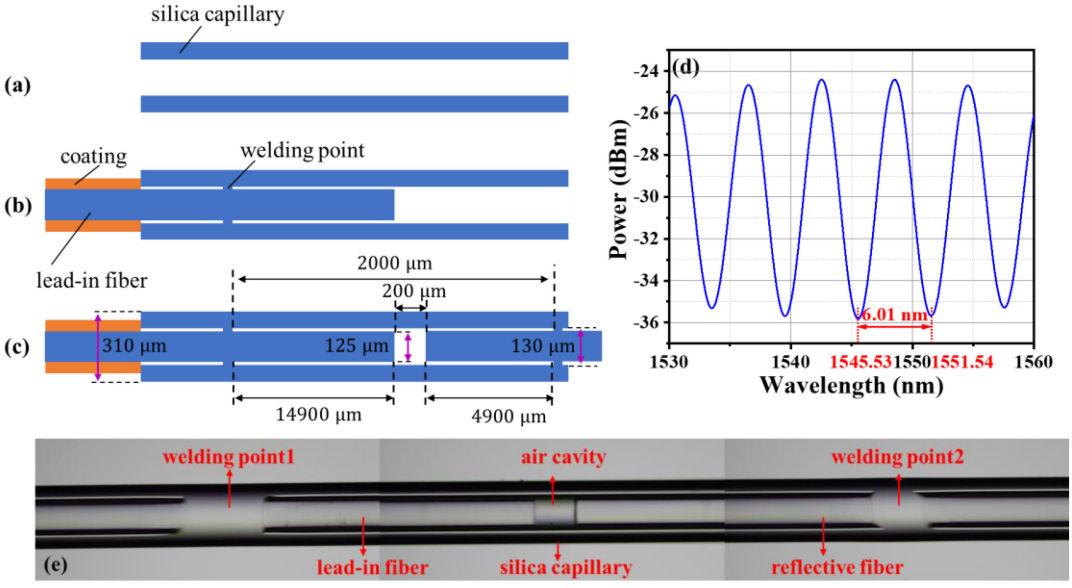

Fig. 3. (a)~(c) The steps of fabricating the pressure sensor; (d) the reflection spectrum and (e) the microscopic photograph of the fabricated pressure sensor.

3. Fabrication of the FPI Sensor

The pressure sensor is mainly fabricated with a CO_2 laser fusion splicer (LZM-100 LAZER Master, Fujikura,30W). When the CO_2 laser is focused on the specific position of the capillary, the capillary material and the fiber cladding are melted by absorbing laser energy. Then, the focused position would be solidified and sealed if the laser is removed. During the welding process, a lead-in fiber is connected to a SM125 (Optical Sensing Interrogator, Micron Optics Inc.) to monitor the reflection spectrum on line.

As displayed in Figs. 3(a), 3(b) and 3(c), the FP cavity fabrication process can be divided into 5 steps: the first step is removing the coating around the capillary, cutting the capillary into the certain length with a cutter afterwards; Secondly, removing the same length coating on SMF as the capillary did, cleaving SMF with a fixed length using a fiber cleaver (CT 30, Fujikura); Thirdly,

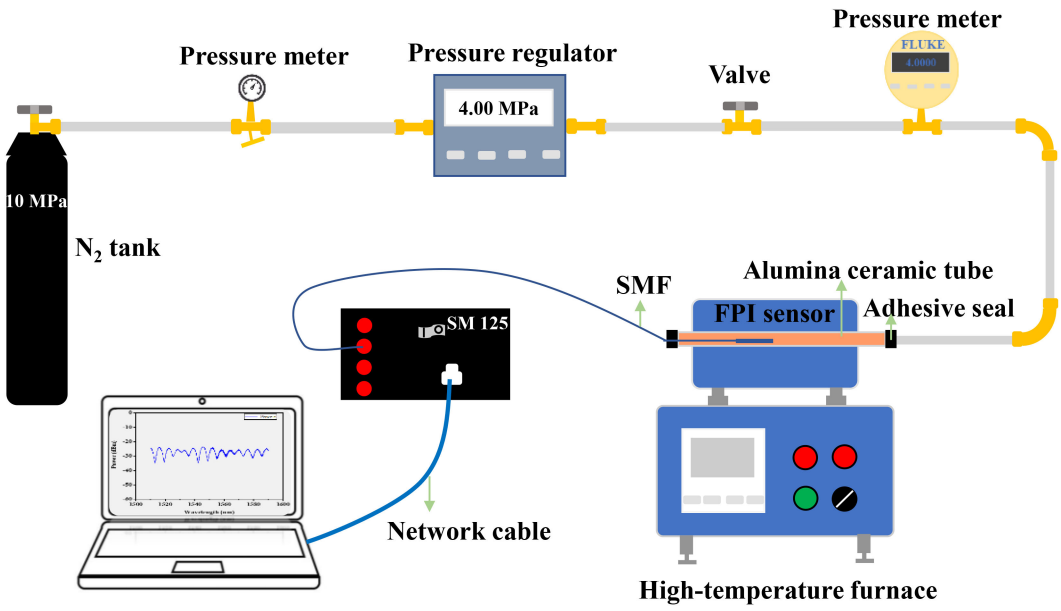

Fig. 4. The schematic diagram of a high-temperature pressure measurement system for the all-silica sensor.

inserting the cleaved fiber into the capillary, fixing the capillary with fiber on the left holder (EV 400, Fujikura) of the CO_2 laser fusion splicer then. Next, welding the fiber and the capillary at the specific position, a certain distance away from the fiber end face by manual operation. Finally, preparing the other cleaved fiber and holding it on the right fixer (EV 250, Fujikura). Inserting the fiber on the right into the capillary and forming a fixed FP cavity length 200 μm and welding the capillary and fiber at a fixed position away from the right fiber end face. After those steps above, the sensor has been fabricated with the cavity length of 200 μm and an approximate fusion-point distance of 2 cm. As displayed in Fig. 3(e), the capillary and the fiber have been welded together at welding positions. As shown in Fig. 3(d), the reflection spectrum is acquired with FSR of 6.01 nm, which is the same as the theoretical value 6.01 nm.

The fusion quality is mainly affected by the temperature of the welding region. The silica fiber and the capillary would become melted to be welded together only if the temperature of the welding region reached a specific value, which is determined by both the laser power and the fusion time. Thus, the laser power and the fusion time should be properly controlled to guarantee a required high temperature for a high fusion quality. Here, the power of the CO_2 laser is properly set as 300 bit and the fusion time is around 19.5 s, respectively. Note that, if the size of the capillary changes, the laser power and the fusion time should be also altered.

4. Experiment and Results

Fig. 4 shows the schematic diagram of a high-temperature pressure measurement system for the all-silica sensor. A pressure regulator (QY-C1-10-Y, resolution $\pm$0.02 MPa) is used to control the delivered gas pressure. To calibrate the delivered pressure, a digital pressure meter (700G08, Fluke) is utilized with a resolution of 0.0001 MPa. Then, the FPI sensor is placed in a sealed Alumina ceramic tube. The reflection spectrum was monitored by a spectrum analyzer (SM125, resolution $\pm$5 pm) ranging from 1510 nm to 1590 nm.

The pressure test experiment was carried out from 25°C to 700°C with a step of 100°C. The gas pressure ranged from standard atmosphere pressure to 4 MPa with a step of 0.5 MPa. At each

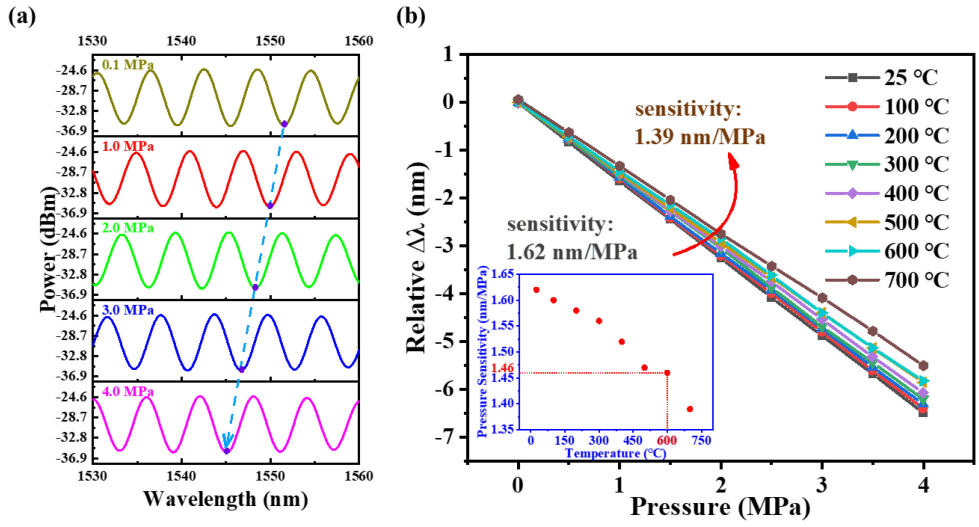

Fig. 5. (a) The spectrum shift at 25°C from standard atmosphere pressure to 4 MPa with a step of 1 MPa; (b) the pressure test results from 25°C to 700°C with a step of 100°C.

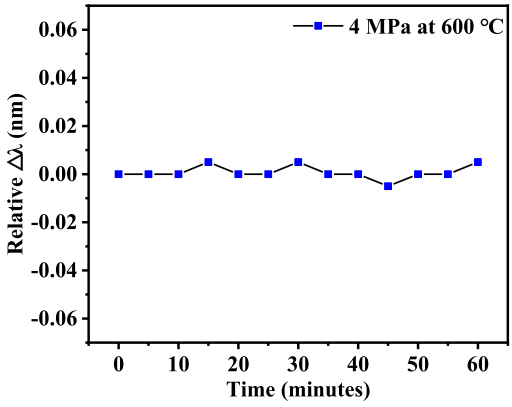

Fig. 6. The relative $\Delta\lambda$ of the pressure sensor at 600°C for an hour.

test, the gas pressure was maintained for 5 minutes to make sure that the gas pressure was stable and the data recorded was accurate. Fig. 5(a) is the spectrum recorded at 25°C from standard atmosphere pressure to 4 MPa with a step of 1 MPa. And Fig. 5(b) shows that the wavelength shift response versus the gas pressure is linear and blue shifted at different test temperatures from standard atmosphere pressure to 4 MPa.

From Fig. 5(b), one can find that the pressure sensitivity decreases from 1.62 nm/MPa to 1.39 nm/MPa with the temperature increasing from 25°C to 700°C, which as agree with the simulation. The insert of Fig. 5(b) shows the decreasing trend of the pressure sensitivity with the temperature increasing. And the pressure sensitivity at 600°C could be obtained as 1.46 nm/MPa. Note that the pressure sensitivity at 25°C in experiment (1.62 nm/MPa) is less than that in simulation (1.74 nm/MPa). The reason is that the fusion-point length of the sensor is 200 μm$\sim$300 μm, which results in the fusion-point distance L_g of less than the set value of 2 cm.

The stability of the FPI pressure sensor was then tested at 600°C under 4 MPa gas pressure for an hour, and the reflection spectrum was recorded in every 5 minutes. Fig. 6 is the pressure stability result with a maximum relative $\Delta\lambda$ fluctuation $\pm$0.005 nm. The maximum zero drift d_z is

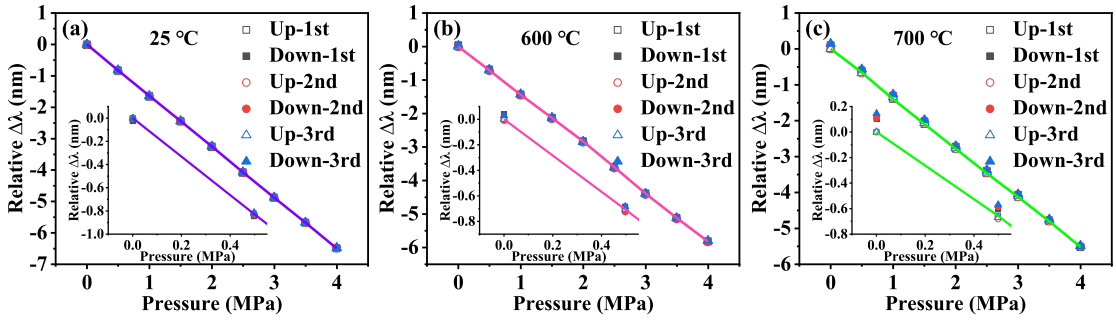

Fig. 7. Three rounds of pressure test results at (a) 25°C, (b) 600°C, and (c) 700°C.

0.085% F.S./h calculated by Eq. (8) [21],

$$d_z = \frac{|y_i - y_o|}{y_{FS}} \times 100\% \tag{8}$$

where y_i is the data recorded in every 5 minutes; y_o is the original value; y_{FS} is the full-scale (F.S.) wavelength shift under 4 MPa at 600°C.

To verify the repeatability and stability of the FPI pressure sensor, three rounds of pressure tests were carried out from room temperature (25°C) to 700°C with a step of 100°C. As displayed in Fig. 7, the experimental results indicate that the pressure response is linear with the wavelength shift at 25°C, 600°C and 700°C. The inserted graphs are the partial enlarged details. From the insert of Fig. 7, the repeatability at 25°C and 600°C is better than that at 700°C. In order to quantify the repeatability, ξ_R is introduced, which can be worked out according to Eq. (9) from the three rounds of pressure test results.

$$\xi_R = \frac{3}{y_{FS}} \cdot \sqrt{\frac{1}{2m}\left(\sum_{i=1}^{m} s_{Ii}^2 + \sum_{i=1}^{m} s_{Di}^2\right)} \tag{9}$$

where m is the number of the pressure test points, $s_{Ii} = \sqrt{\frac{1}{n-1}\sum_{j=1}^{n}(y_{Iij} - \overline{y}_{Ii})^2}$ and $s_{Di} = \sqrt{\frac{1}{n-1}\sum_{j=1}^{n}(y_{Dij} - \overline{y}_{Di})^2}$ are the standard deviation at each measured point with the pressure increasing or decreasing. n is the number of the pressure test round. y_{Iij} and y_{Dij} are the obtained results of the ith pressure test point in the jth round of pressure test with the pressure increasing or decreasing. $\overline{y}_{Ii}$ and $\overline{y}_{Di}$ are the mean results of the ith test point during the n rounds of pressure tests.

In Fig. 8(a), the repeatability is measured as 0.36% at 25°C, 0.83% at 600°C and 0.89% at 700°C, respectively. It indicates that the repeatability becomes worse with the temperature increasing.

In order to evaluate the pressure sensor's performance, the 700G08-FLUKE pressure meter was tested for comparison. To minimize the experimental error, the linear working equation of the pressure sensor is determined by three rounds of pressure test results obtained before. Fig. 9 shows the results calculated from the linear working equation (estimated by the linear least square method) and the results acquired by the 700G08-FLUKE pressure meter. The total error is another parameter to verify the pressure sensor, which can be calculated by Eq. (10).

$$A = \pm\left(\frac{|\Delta y_{LH}|_{\max}}{y_{FS}} + \xi_R\right) \tag{10}$$

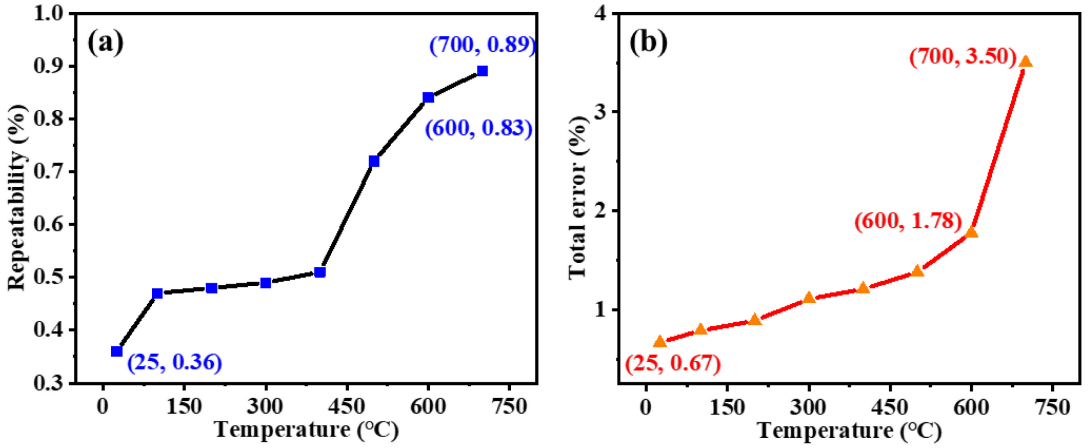

Fig. 8. (a) The repeatability and (b) total error of the pressure sensor from 25°C to 700°C.

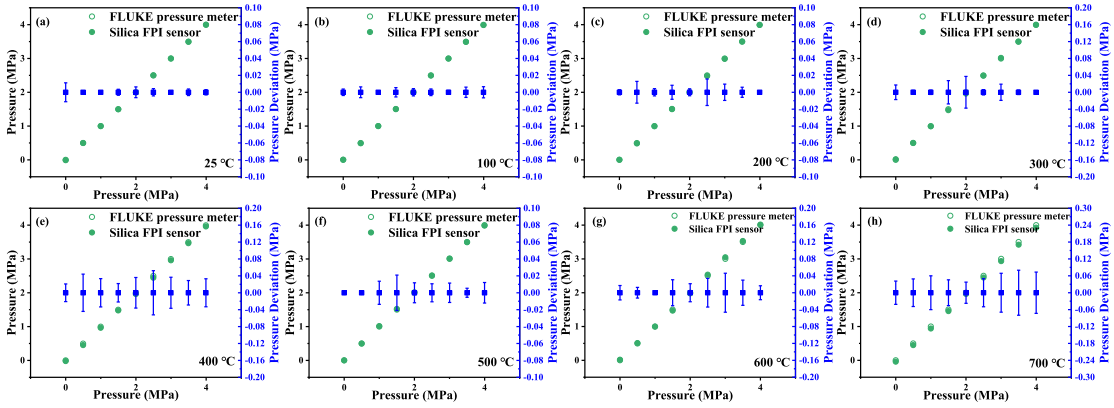

Fig. 9. The working equation of the FPI sensor compared with the data acquired by pressure meter at (a) 25 °C, (b) 100 °C, (c) 200 °C, (d) 300 °C, (e) 400 °C, (f) 500 °C, (g) 600 °C and (h) 700 °C.

where $(\Delta y_{LH})_i = \bar{y}_i - y_{EPi}$ is the differences between the mean results ($\bar{y}_i$) of three rounds of pressure tests and the ith test results (y_{EPi}) calculated by the sensor's linear working equation. As displayed in Fig. 8(b), the total error is ±0.67% at 25°C, ±1.78% at 600°C and ±3.50% at 700°C. Thus, the FPI sensor is more suitable for the temperature less than 600°C in order to realize the pressure test with relatively low error (<±2%).

From the results obtained above, one can find that both the repeatability and the total error increase with the increased temperature. This phenomenon could be explained from three perspectives: (i) the pressure sensitivity and the maximum wavelength shift y_{FS} decrease with the increased temperature because of the increase of the Young's modulus E in Eq. (2); (ii) the thermal expansion coefficient of the fiber core is larger than that of the cladding, so the fiber facet would become rougher under high temperature, which would increase the error when light experiences multiple reflections between two fiber facets; (iii) the mechanical properties of the silica material becomes unstable as the temperature increases. Residual stress around the welding points of the sensor will be released under the high temperature, which hence affects the consistency of the obtained sensing data. Furthermore, the silica material of the pressure sensor would generate plastic deformation when applying and removing the pressure under high temperature.

5. Conclusion

We have demonstrated an all-silica FPI high-temperature pressure sensor, in which the influence of the temperature on pressure sensing is investigated. Results show that the pressure sensitivity decreases from 1.62 nm/MPa at 25°C to 1.39 nm/MPa at 700°C. Thanks to the CO_2 laser bonding method without any other adhesive, the sensor has a good repeatability and stability up to 600°C with a pressure sensitivity of 1.46 nm/MPa, a repeatability of 0.83% and a total error of $\pm$1.78%, respectively. The sensor has the advantages of stably working performance, batch fabrication and low cost, suggesting promising application in high-temperature environment.

References

[1] B. H. Lee *et al.*, "Interferometric fiber optic sensors," *Sensors*, vol. 12, no. 3, pp. 2467–2486, 2012.
[2] S. H. Aref, H. Latifi, M. I. Zibaii, and M. Afshari, "Fiber optic Fabry-Pérot pressure sensor with low sensitivity to temperature changes for downhole application," *Opt. Commun.*, vol. 269, no. 2, pp. 322–330, Aug. 2006.
[3] T. Zhu, D. Wu, M. Liu, and D. W. Duan, "In-line fiber optic interferometric sensors in single-mode fibers," *Sensors*, vol. 12, no. 8, pp. 10430–10449, Aug. 2012.
[4] V. Bhatia *et al.*, "Optical fiber based absolute extrinsic Fabry-Pérot interferometric sensing system," *Meas. Sci. Technol.*, vol. 7, no. pp. 1 pp. 58–61, Oct. 1996.
[5] Y. J. Rao, M. Deng, D. W. Duan, X. C. Yang, T. Zhu, and G. H. Cheng, "Micro Fabry-Pérot interferometers in silica fibers machined by femtosecond laser," *Opt. Exp.*, vol. 15, no. 21, pp. 14123–14128, Oct. 2007.
[6] Y. J. Rao, M. Deng, T. Zhu, and H. Li, "In-line Fabry-Pérot etalons based on hollow-core photonic bandgap fibers for high-temperature applications," *J. Lightw. Technol.*, vol. 27, no. 19, pp. 4360–4365, Oct. 2009.
[7] Y. Wang, D. N. Wang, C. R. Liao, T. Y. Hu, J. T. Guo, and H. F. Wei, "Temperature-insensitive refractive index sensing by use of micro Fabry-Pérot cavity based on simplified hollow-core photonic crystal fiber," *Opt. Lett.*, vol. 38, no. 3, pp. 269–271, Feb. 2013.
[8] R. Oliveira, L. Bilro, R. Nogueira, and A. M. Rocha, "Adhesive based Fabry-Pérot hydrostatic pressure sensor with improved and controlled sensitivity," *J. Lightw. Technol.*, vol. 37, no. 9, pp. 1909–1915, May 2019.
[9] B. Sun *et al.*, "Simultaneous measurement of pressure and temperature by employing Fabry-Pérot interferometer based on pendant polymer droplet," *Opt. Exp.*, vol. 23, no. 3, pp. 1906–1911, Jan. 2015.
[10] X. L. Zhou, Q. X. Yu, and W. Peng, "Fiber-optic Fabry-Pérot pressure sensor for down-hole application," *Opt. Laser Eng.*, vol. 121, pp. 289–299, May 2019.
[11] Q. C. Zhao *et al.*, "Adhesive-free bonding fiber optic Fabry-Pérot pressure sensor based on oxy-hydrogen flame welding and spiral tube," *Opt. Commun.*, vol. 476, Jul. 2020, Art. no. 126307.
[12] C. R. Liao *et al.*, "Sub-micron silica diaphragm-based fiber-tip Fabry-Pérot interferometer for pressure measurement," *Opt. Lett.*, vol. 39, no. 10, pp. 2827–2830, Apr. 2014.
[13] Z. Li *et al.*, "Microbubble-based fiber-optic Fabry-Pérot pressure sensor for high-temperature application," *Appl. Opt.*, vol. 57, no. 8, pp. 1738–1743, Mar. 2018.
[14] J. Liu, Y. Z. Sun, and X. D. Fan, "Highly versatile fiber-based optical Fabry-Pérot gas sensor," *Opt. Exp.*, vol. 17, no. 4, pp. 2731–2738, Feb. 2009.
[15] C. L. Lee, J. M. Hsu, J. S. Horng, W. Y. Sung, and C. M. Li, "Microcavity fiber Fabry-Pérot interferometer with an embedded golden thin film," *IEEE Photon. Tech. Lett.*, vol. 25, no. 9, pp. 833–836, May 2013.
[16] W. P. Chen, D. N. Wang, B. Xu, C. L. Zhao, and H. F. Chen, "Multimode fiber tip Fabry-Pérot cavity for highly sensitive pressure measurement," *Sci. Rep.*, vol. 7, no. 1, pp. 1–6, Mar. 2017.
[17] Y. N. Zhang, L. Yuan, X. W. Lan, A. Kaur, J. Huang, and H. Xiao, "High-temperature fiber-optic Fabry-Pérot interferometric pressure sensor fabricated by femtosecond laser," *Opt. Lett.*, vol. 38, no. 22, pp. 4609–4612, Nov. 2013.
[18] C. R. Liao, T. Y. Hu, and D. N. Wang, "Optical fiber Fabry-Pérot interferometer cavity fabricated by femtosecond laser micromachining and fusion splicing for refractive index sensing," *Opt. Exp.*, vol. 20, no. 20, pp. 22813–22818, Sep. 2012.
[19] B. Qi *et al.*, "Fiber optic pressure and temperature sensors for oil down hole application," *Proc. SPIE*, vol. 4578, pp. 182–190, 2002.
[20] Y. Y. Wang, C. Wang, X. H. Liu, and Q. C. Zhao, "Research on optical fiber grating sensor based on Fabry-Pérot cavity applied in oilfield," *Appl. Mech. Mater.*, vol. 336, pp. 153–157, Jul. 2013.
[21] X. Y. Sheng, X. W. Li, H. Y. Wang, Z. P. Lv, G. C. Zhang, J. P. Yan, and H. Wu, "Verification Regulation of Pressure Transducer (Static) JJG 860-2015," *General Admin. of Qual. Supervision, Inspection and Quarantine of the People's Republic of China*, pp. 1–16, Jul. 2015.